Supporting Information

Cu clusters/TiO$_{2-x}$ with abundant oxygen vacancies for enhanced electrocatalytic nitrate reduction to ammonia

Xi Zhang,‡[a] Changhong Wang,‡[a] Yamei Guo,[a] Bin Zhang,[a, b] Yuting Wang,*[a] Yifu Yu*[a, c]

[a] *Department of Chemistry, School of Science, Institute of Molecular Plus, Tianjin University, Tianjin 300072, China*

[b] *Tianjin Key Laboratory of Molecular Optoelectronic Science, Collaborative Innovation Center of Chemical Science and Engineering, Tianjin 300072, China*

[c] *Haihe Laboratory of Sustainable Chemical Transformations, Tianjin 300192, China*

E-mail addresses: wangyuting@tju.edu.cn; yyu@tju.edu.cn

‡ The authors contributed equally.

1. Experimental Procedures

1.1 Synthesis of TiO$_2$.

TiO$_2$ nanosheets were synthesized through a previous solvothermal method.[1] First, 3 mL of hydrofluoric acid solution (40 wt%) was added dropwise to 25 mL of Ti(OBu)$_4$•(TBOT) under stirring, and then the mixture turns to a gel. Second, the obtained gel was transferred into a dried Teflon autoclave and heated at 180 °C for 36 h. Third, the sample was separated from the suspension, and washed with ethanol and deionized water for several times. Forth, the sample was dispersed in 50 mL of 0.1 M NaOH aqueous, and then vigorously stirred for 10 h at room temperature. Finally, TiO$_2$ nanosheets could be obtained after washing with deionized water and ethanol for several times, and then drying under vacuum overnight.

1.2 Synthesis of 10Cu/TiO$_{2-x}$.

10Cu/TiO$_{2-x}$ was synthesized according to the impregnation method, followed by the H$_2$ treatment. 50 mg of TiO$_2$ nanosheet powder was evenly dispersed in 20 mL of ethanol and stirred for 30 min, a certain amount of dissolved CuSO$_4$·5H$_2$O was added dropwise to the suspension. After vigorously stirring for 6 h at room temperature, the sample was separated from the suspension, and annealed in a reducing atmosphere (3 vol.% H$_2$ and 97 vol.% Ar) at 300 °C for 2 h with a heating rate of 5 °C min^{-1}. Other samples with different loading amounts (0, 1, 5, 15 wt%) were prepared through the same synthetic procedures except that amount of CuSO$_4$·5H$_2$O was changed.

1.3 Synthesis of 10Cu/TiO$_2$.

10Cu/TiO$_2$ was synthesized via the NaBH$_4$ reduction method.[2] Typically, 50 mg of TiO$_2$ nanosheet powder was evenly dispersed in 200 mL of deionized water and stirred for 30 min. Ar gas was purged for 30 min to remove the air in the solution, and then a certain amount of dissolved CuSO$_4$·5H$_2$O was added dropwise to the suspension. After vigorously stirring for 3 h at room temperature, 50 mg NaBH$_4$ in 5 mL water was injected into the above solution at a rate of 2 ml min^{-1}. The final product was obtained by centrifugation with deionized water and ethanol several times, and then dried under vacuum overnight.

1.4 Pre-treatment of carbon paper (CP).

The CP was firstly cut into rectangles with an area of 3 cm × 1 cm, and then ultrasonicated with ethanol for 10 min. After rinsing with ultrapure water, CPs were heated at 60 °C for 24 h with a mixture of water, concentrated sulfuric acid and concentrated nitric acid (volume ratio 1:1:1). At last, CPs were washed with ultrapure water for further use.

1.5 Characterization.

Scanning electron microscopy (SEM) was obtained using a FEI Apreo S LoVac scanning electron microscope. Transmission electron microscopy (TEM), high-resolution TEM (HRTEM), and scanning transmission electron microscopy-energy dispersive spectroscopy (STEM-EDS) elemental mapping were conducted using a JEOL JEM-200F microscope. X-ray diffraction (XRD) was measured at the Rigaku Smartlab9KW Diffraction System using a Cu Kα source ($\lambda = 0.15406$ nm), and the diffraction data was recorded in the 2θ range of $20 \sim 80^o$ with a scan rate of 10° min^{-1}. Electron paramagnetic resonance (EPR) measurements were obtained using a Bruker EMXPLUS. X-ray photoelectron spectroscopy (XPS) analysis was performed with a ThermoFisher Scientific ESCALAB Xi+ spectrometer with Al Kα excitation source. All binding energies were corrected with the C 1s peak at 284.8 eV. Inductively Coupled Plasma Optical Emission Spectrometry (ICP-OES) was performed using Agilent 5110. The ultraviolet-visible (UV-Vis) absorbance spectra were measured on Beijing Purkinje General T6 new century spectrophotometer. The ^{1}H nuclear magnetic resonance (NMR) spectra were measured on a JEOL JNM ECZ600R.

1.6 Electrochemical measurements.

1.6.1 Preparation of the working electrode. Typically, 1 mg of catalyst powder was dispersed in a mixed solvent containing 0.5 mL of ethanol and 10 μL of 5% Nafion solution. After ultrasonic treatment for 20 min, the catalyst slurry was dropped uniformly onto a piece of CP with a size of 1 cm × 1 cm to obtain a working electrode.

1.6.2 Electrochemical nitrate reduction experiment. The electrochemical test was performed on a CHI 660D electrochemical workstation, using an H-cell system separated by a Nafion 117 membrane. Catalyst-coated carbon paper, carbon rod and saturated calomel electrode (SCE) were used as working, counter, and reference electrodes, respectively. The electrolyte used in this work was 0.5 M Na$_2$SO$_4$ solution (80 mL), which was evenly distributed to the cathodic and anodic chamber. NaNO$_3$ (200 ppm NO$_3^-$-N) was added into the cathodic chamber as the reactant. Magnetic stirring was applied with a stirring rate of 350 rpm in the cathodic chamber during the electrochemical test. All potentials were recorded against the reversible hydrogen electrode (RHE) without special explanation. The linear sweep voltammetry (LSV) test was performed at a rate of 10 mV s^{-1}, and potentiostatic electrolysis was conducted at each potential for 2 h. Differential electrochemical mass spectrometry (DEMS) was provided by Linglu instruments (Shanghai) Co. Ltd. Electrochemical *in situ* FTIR spectroscopy was

carried out on a Nicolet Nexus 670 spectrometer using a mercury-cadmium-telluride (MCT) detector cooled by liquid nitrogen.

1.7 Ion concentration detection methods.

The ion concentration was quantified by the UV-Vis spectrophotometer, after diluting to an appropriate concentration based on the calibration curves. The specific detection methods are as follows.

Detection of nitrate-N. Firstly, a certain amount of electrolyte was extracted from the cathodic chamber and diluted to 5 mL to detection range. Then, 10 μL of 0.8 w% sulfamic acid solution and 0.1 mL of 1 M HCl were subsequently added into the above solution and mixed uniformity. After standing at room temperature for 20 min, the absorbance was recorded at a wavelength of 220 nm and 275 nm using an UV-Vis spectrophotometer. The final absorbance value was calculated according to the equation: $A = A_{220\ nm} - 2A_{275\ nm}$. The concentration-absorbance curve was calibrated using the standard $NaNO_3$ with different NO_3^--N concentrations.

Detection of nitrite-N. A mixture of p-aminobenzenesulfonamide (4 g), N-(1-Naphthyl) ethylenediamine dihydrochloride (0.2 g), ultrapure water (50 mL) and phosphoric acid (10 mL, 1.70 g mL^{-1}) was used as a color reagent. A certain amount of electrolyte was extracted from the cathodic chamber and diluted to 5 mL to detection range. Then, 0.1 mL of color reagent was added into the above solution and mixed uniformity. After standing at room temperature for 20 min, the absorbance was recorded at a wavelength of 540 nm. The concentration-absorbance curve was calibrated using the standard $NaNO_2$ with different NO_2^--N concentrations.

Detection of ammonia-N. The Nessler's reagent was used as the color reagent for the determination of ammonia-N. Firstly, a certain amount of electrolyte was extracted from the cathodic chamber and diluted to 5 mL to detection range. Then, 0.1 mL of potassium sodium tartrate solution ($\rho = 500$ g L^{-1}) and 0.1 mL Nessler's reagent were subsequently added into the above solution and mixed uniformity. After standing at room temperature for 20 min, the absorbance was recorded at a wavelength of 420 nm. The concentration-absorbance curve was calibrated using the standard $(NH_4)_2SO_4$ with different NH_4^+-N concentrations.

1.8 Isotope labeling experiments.

Before the isotope labeling experiment, the calibration curve was created. First, a series of standard solutions ($(^{15}NH_4)_2SO_4$) with known concentration were prepared in 0.5 M Na_2SO_4 solution with 100 ppm of maleic acid ($C_4H_4O_4$) as internal standard. Second, the standard solutions were acidized to pH ~

1 with 4 M H_2SO_4. Third, 50 μL of deuterium oxide (D_2O) was added in 0.5 mL above solution for the

^1H NMR (600 MHz) detection. Fourth, the standard curve was obtained according to the integral area of

$^{15}NH_4^+$-^{15}N/$C_4H_4O_4$ against concentration of $^{15}NH_4^+$-^{15}N. The isotopic labeling experiment was

conducted via the electrochemical procedure (see 2.3.2. section in manuscript for details), except that

$Na^{15}NO_3$ (99.21%) was used as the reactant. After 2 h of electrolysis on $10Cu/TiO_{2-x}$ at the applied

potential of -0.75 V vs. RHE, the obtained $^{15}NH_4^+$ was quantified by ^1H NMR (600 MHz). Similarly, the

calibration curve of $^{14}NH_4^+$-^{14}N was established, and the concentration of $^{14}NH_4^+$ was quantified with

$Na^{14}NO_3$ as the nitrogen source.

1.9 Calculation of the conversion rate, selectivity, Faradaic efficiency, and the yield rate.

The conversion rate was calculated according to the Eq. S1:

$$\text{Conversion} = \Delta c_{NO_3^-} / c_0 \times 100\% \tag{Eq. S1}$$

The selectivity to ammonia and nitrite were obtained by the Eq. S2-3:

$$S_{NH_3} = c_{NH_3} / \Delta c_{NO_3^-} \times 100\% \tag{Eq. S2}$$

$$S_{NO_2^-} = c_{NO_2^-} / \Delta c_{NO_3^-} \times 100\% \tag{Eq. S3}$$

The FE was defined from the charge consumed for NH_3 synthesis and total charge passed through the

electrode:

$$FE = (8F \times c_{NH_3} \times V) / (M_{NH_3} \times Q) \tag{Eq. S4}$$

The yield rate was obtained by the Eq. S5:

$$\text{Yield}_{NH_3} = (c_{NH_3} \times V) / (M_{NH_3} \times t \times S) \tag{Eq. S5}$$

Where $\Delta c_{NO_3^-}$ is the concentration difference of NO_3^- before and after electrolysis, c_0 is the initial

concentration of NO_3^-, $c_{NO_3^-}$ is the mass concentration of NO_3^-, c_{NH_3} is the produced mass concentration

of NH_3, $c_{NO_2^-}$ is the produced mass concentration of NO_2^-, M_{NH_3} is the molar mass of NH_3, F is the

Faradaic constant (96485 C mol^{-1}), Q is the quantity of applied electricity, V is the volume of electrolyte

in the cathode chamber (40 mL), t is the electrolysis time (2 h), S is the geometric area of the working

electrode (1 cm^2).

1.10 Differential electrochemical mass spectrometry measurement.

DEMS measurement was performed on a homemade electrochemical cell equipped with a peristaltic

pump. Catalyst-coated carbon paper, Pt wire, and Ag/AgCl electrode were used as the working, counter electrode, and reference electrodes, respectively. The potentiostatic measurement was adopted. After the baseline remained stable, the potential switch was turned on and off periodically. Four cycles of the mass signals were collected to avoid the accidental errors during the DEMS measurements.

1.11 Electrochemical *in situ* FTIR spectroscopy.

Electrochemical *in situ* FTIR spectroscopy was carried out on a Nicolet Nexus 670 spectrometer using a mercury-cadmium-telluride (MCT) detector cooled by liquid nitrogen. Catalyst-coated Au-modified single bounce silicon, Pt wire, and SCE were used as the working, counter, and reference electrodes, respectively. The potentiostatic measurement technology was adopted.

1.12 Theoretical calculation details

All the computations were performed based on the density functional theory (DFT) methods, as implemented in the plane wave set Vienna ab initio Simulation Package (VASP) code.[3, 4] The exchange-correlation functional in the Perdew-Burke-Ernzerhof (PBE) form within a generalized gradient approximation (GGA) was used.[5] Spin polarization was considered in all calculations. To better describe the on-site coulomb (U) correlation of the localized 3d electrons for transition metal Ti and Cu, the DFT + U method with $U - J = 2.58$ eV for Ti and $U - J = 3.87$ eV for Cu was adopted.[6, 7] The thermodynamic corrections due to the solvent effect (G_{solv}) were calculated by using VASPsol.[8] A kinetic-energy cut off of 500 eV was set. The convergence threshold for the iteration in the self-consistent field (SCF) was set as 10^{-4} eV. The geometry optimization within the conjugate gradient method was performed with forces on each atom less than 0.05 eV/Å. A p(1×3) unit cell of TiO_2 (101) surface with a three-layer model of the crystal plane was used to ensure the lateral lattice lager than 1 nm. One surface O was removed to model the TiO_{2-x} surface. Cu_4 cluster was introduced to TiO_2 and TiO_{2-x} to form the Cu/TiO_2 and Cu/TiO_{2-x} interfaces. To prevent the periodic image interactions, a large vacuum layer of 15 Å was inserted in the z-direction. Bottom two atomic Ti-O layers were fixed while other layers and the adsorbates were fully relaxed during structural optimizations. The Brillouin zone was sampled by a k-point mesh of $4 \times 4 \times 1$. The reaction free energy change can be obtained with the following equation:

$$\Delta G = \Delta E + \Delta E_{ZPE} - T\Delta S$$

where ΔE is the total energy difference between the products and the reactants of each reaction step, and ΔE_{ZPE} and ΔS are the differences of zero-point energy and entropy, respectively. The zero-point energy

of free molecules and adsorbates are obtained from the vibrational frequency calculations. The free energy change of each step that involves an electrochemical proton-electron transfer is described by the computational hydrogen electrode (CHE) model proposed by Nørskov et al.[9] In this technique, zero voltage is defined based on the reversible hydrogen electrode, in which the reaction is defined to be in equilibrium at zero voltage, at all values of pH, at all temperatures, and with H_2 at 101,325 Pa pressure. Therefore, in the CHE model, the free energy of a proton-electron pair is equal to half of the free energy of gaseous hydrogen at a potential of 0 V.

To avoid describing the charged NO_3^- species as a reference within periodic DFT calculations, we used neutral HNO_3 as gas-phase reference instead.[10] The energy for the nitrate ion was obtained by using reference values for the ionization energy of H (*I.E.*) and the heat of reaction for $HNO_3(g)$ deprotonation (ΔH_r).[11]

2. Results and Discussions
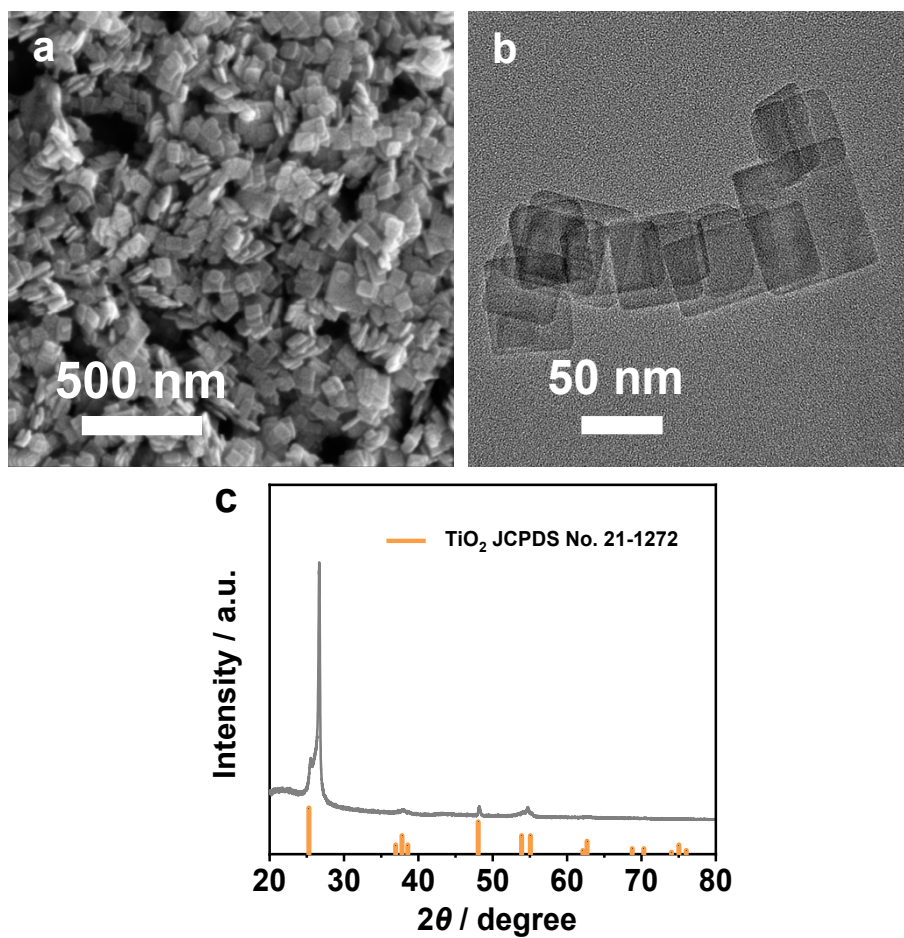
Fig. S1. (a) SEM image, (b) TEM image, (c) XRD pattern of TiO_2.

Both SEM and TEM images show that TiO_2 possesses nanosheet morphology with a size of about 50 nm. The XRD pattern reveals that the diffraction peaks of TiO_2 is well coincident with anatase-type TiO_2 phase (JCPDS No. 21-1272). The addition peaks at around 26° and 54° arise from the CP substrate. (JCPDS: Joint Committee on Powder Diffraction Standards)
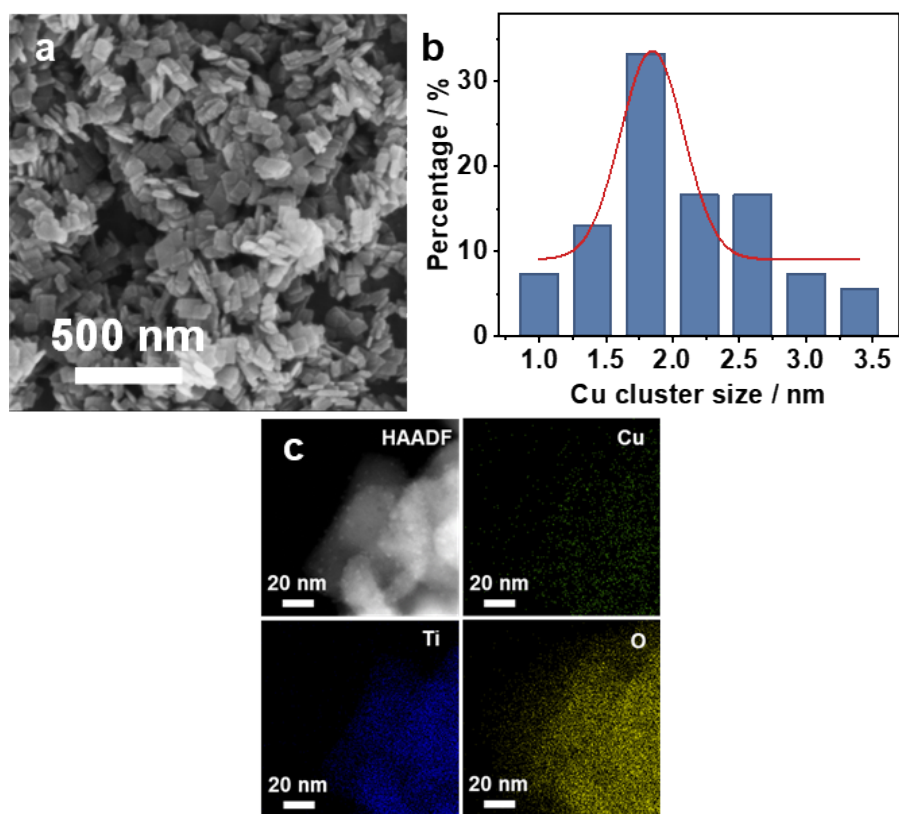
Fig. S2. (a) SEM image, (b) the size distribution of the Cu clusters, (c) STEM-EDS elemental mapping images of $10Cu/TiO_{2-x}$.

SEM image of $10Cu/TiO_{2-x}$ show the maintenance of the nanosheet structure of initial TiO_2. Cu clusters with an average size of 2 nm are loaded on TiO_{2-x} nanosheets.
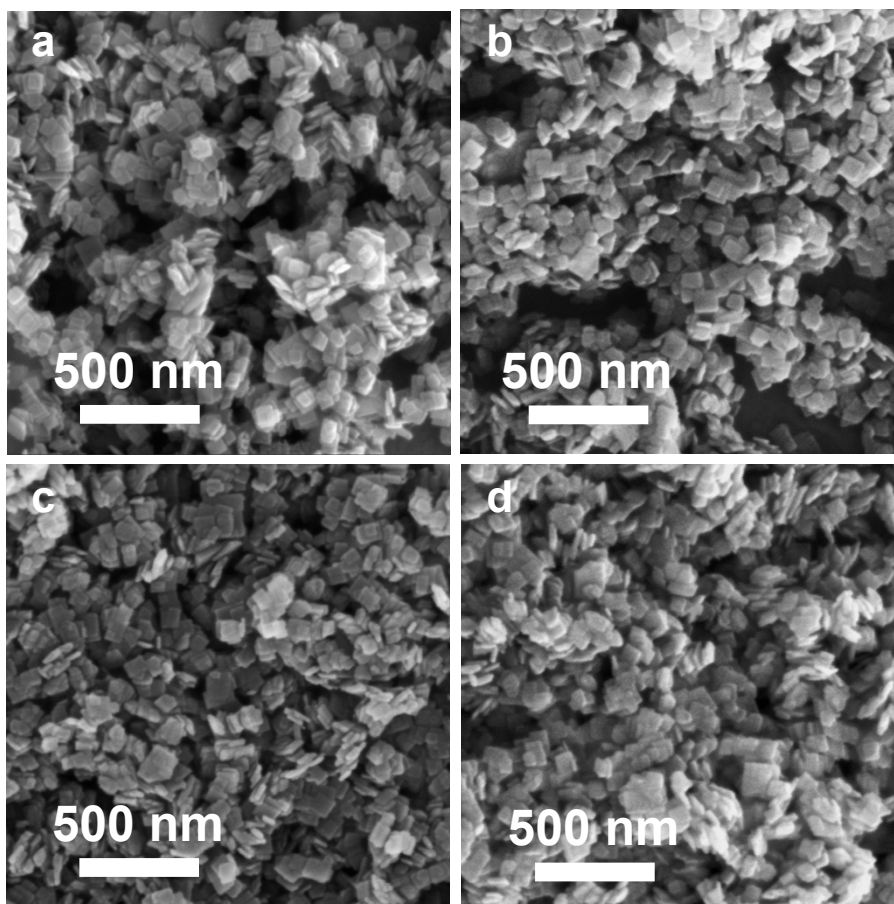
Fig. S3. SEM image of (a) TiO_{2-x}, (b) $1Cu/TiO_{2-x}$, (c) $5Cu/TiO_{2-x}$, (d) $15Cu/TiO_{2-x}$.

SEM images of different samples show the maintenance of TiO_2 nanosheet.
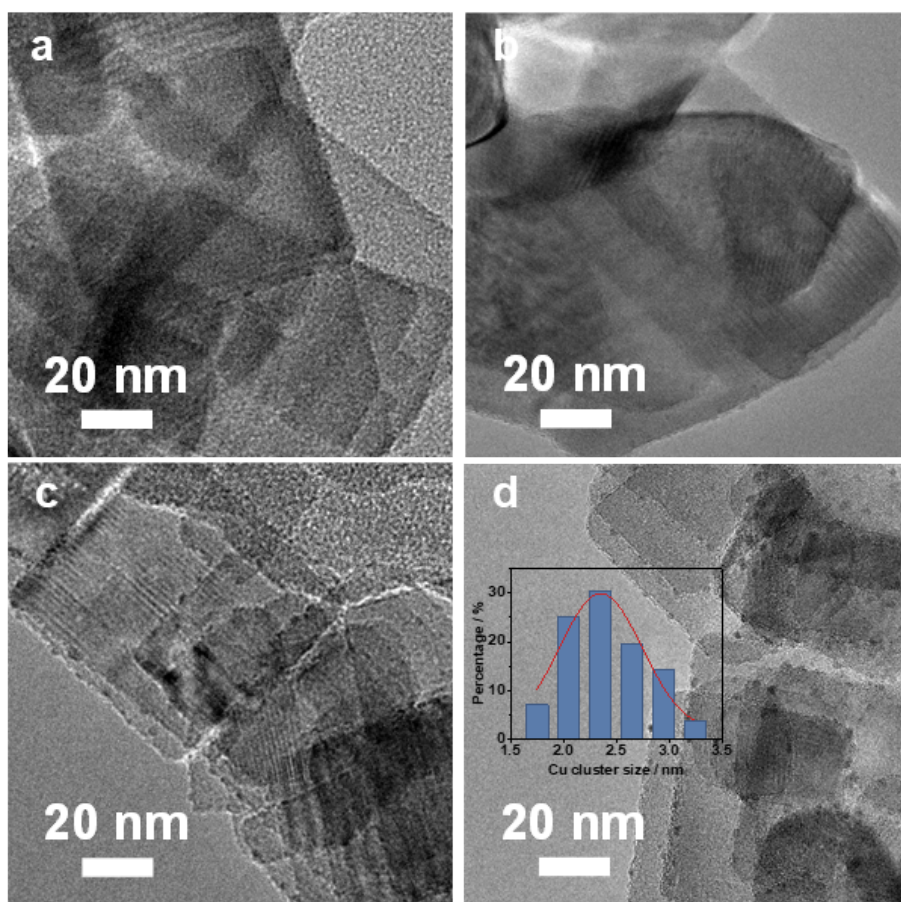
Fig. S4 TEM images of (a) TiO_{2-x}, (b) $1Cu/TiO_{2-x}$, (c) $5Cu/TiO_{2-x}$, (d) $15Cu/TiO_{2-x}$ (inset shows the size distribution of the Cu clusters).

TiO_{2-x} exhibits a similar morphology to TiO_2. $1Cu/TiO_{2-x}$ and $5Cu/TiO_{2-x}$ show a small amount of Cu clusters loaded on TiO_{2-x} NSs. TEM image of $15Cu/TiO_{2-x}$ catalyst shows that Cu clusters with a diameter of ~2.4 nm are loaded on the surface of TiO_{2-x} NSs.
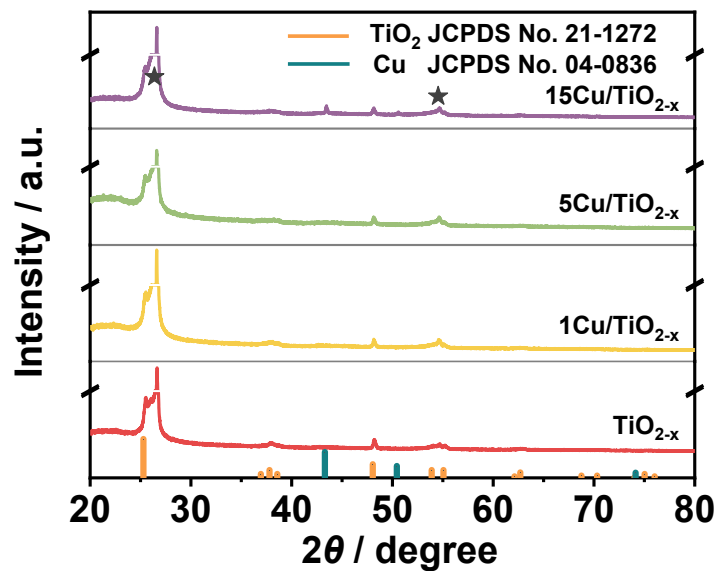
Fig. S5. XRD patterns of TiO_{2-x}, $1Cu/TiO_{2-x}$, $5Cu/TiO_{2-x}$ and $15Cu/TiO_{2-x}$.

The anatase-type TiO_2 (JCPDS No. 21-1272) can be identified in XRD patterns for different samples.

Obvious diffraction peaks indexed to Cu (JCPDS No. 04-0836) can be found in $15Cu/TiO_{2-x}$ catalyst.
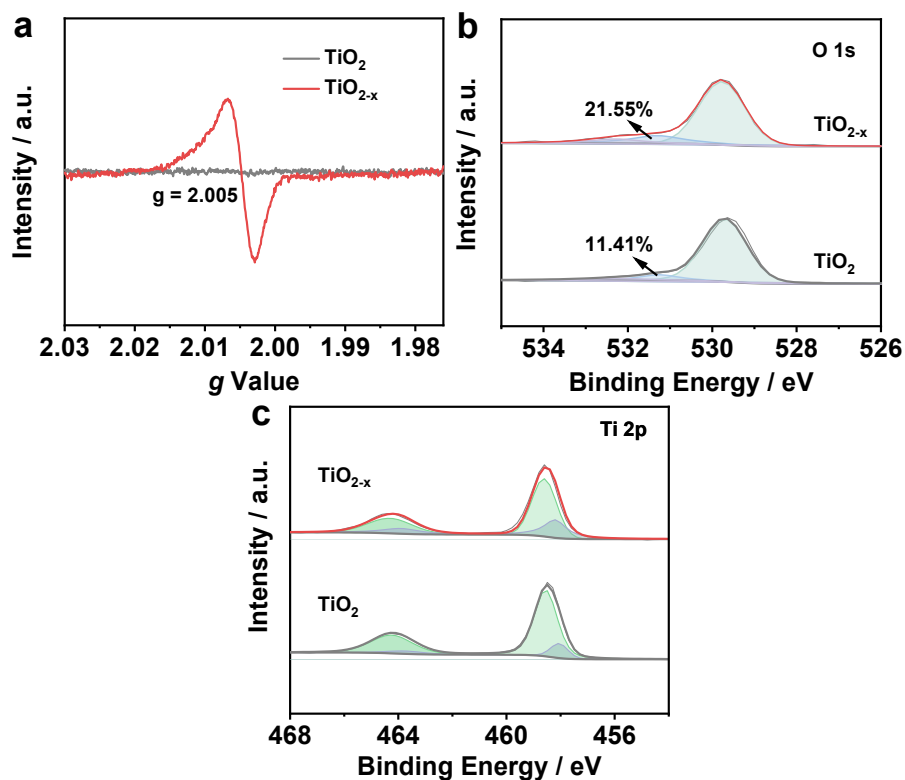
Fig. S6. (a) EPR spectra, (b) O 1s XPS spectra, (c) Ti 2p XPS spectra of TiO_{2-x} and TiO_2.

According to the EPR results, a stronger resonance signal at g = 2.005 is observed on TiO_{2-x} compared to TiO_2. The peak area ratio of oxygen vacancy relative to metal-oxygen bonds is 21.55% and 11.41% for TiO_{2-x} and TiO_2, respectively. The larger OV fraction of the peak at ~531.3 eV in TiO_{2-x} suggests higher concentration of OVs. In addition, the percentage of Ti^{3+} in $2p_{3/2}$ region of TiO_{2-x} is higher than that of TiO_2. Therefore, it is revealed that OVs are successfully created in TiO_{2-x}.
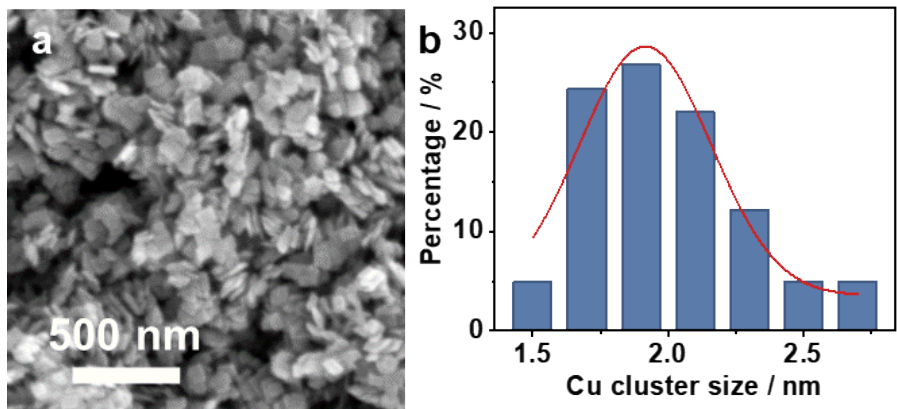
Fig. S7. (a) SEM image of $10Cu/TiO_2$. (b) The distribution of the Cu clusters in $10Cu/TiO_2$.

The structure of TiO_2 after anchoring Cu clusters maintain as shown in SEM image, and Cu clusters with

an average size of 2 nm are shown in $10Cu/TiO_2$, indicating a similar morphology to $10Cu/TiO_{2-x}$.

x.
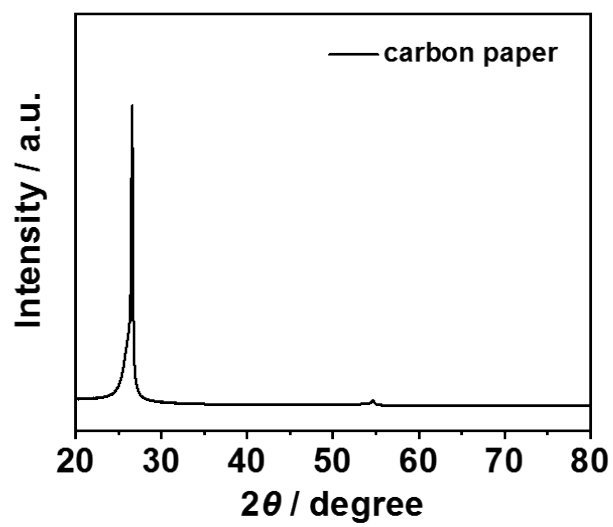
Fig. S8. XRD pattern of carbon paper.
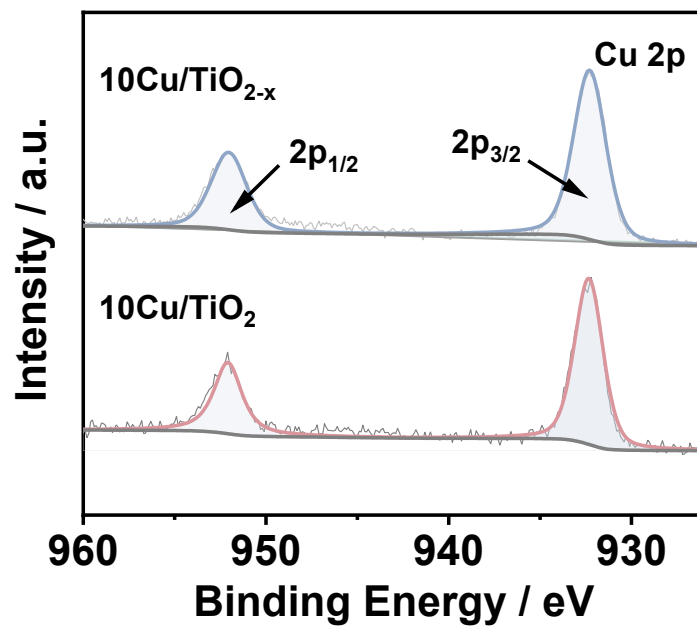
Fig. S9. Cu 2p XPS spectra of 10Cu/TiO$_{2-x}$ and 10Cu/TiO$_2$.

The two peaks centered at ~932.4 and ~952.1 eV can be assigned to the Cu 2p$_{3/2}$ and Cu 2p$_{1/2}$, respectively. Combined with the XRD results, it is typical for the Cu^0 clusters supported on TiO$_{2-x}$ and TiO$_2$.
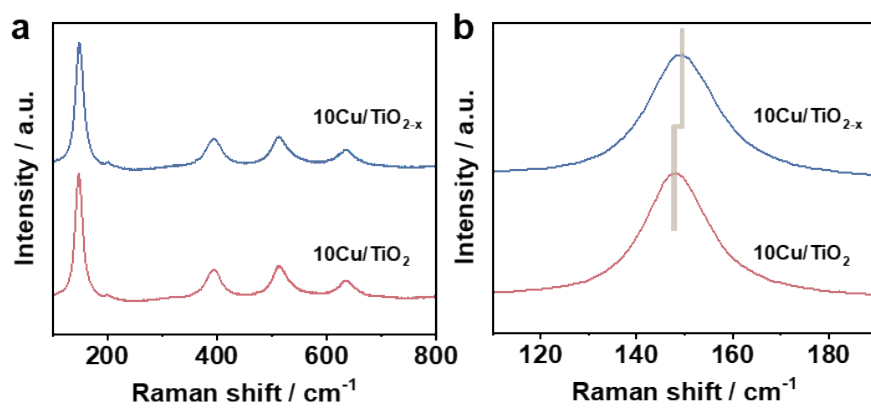
Fig. S10. (a) Raman spectra of 10Cu/TiO$_{2-x}$, and 10Cu/TiO$_2$. (b) The enlarged Raman peaks of 10Cu/TiO$_{2-x}$, and 10Cu/TiO$_2$.

Notably, the main peak at ~146 cm^{-1} in 10Cu/TiO$_{2-x}$ sample broadens and shifts to a higher wavenumber compared with 10Cu/TiO$_2$, further indicating the presence of OVs in 10Cu/TiO$_{2-x}$.
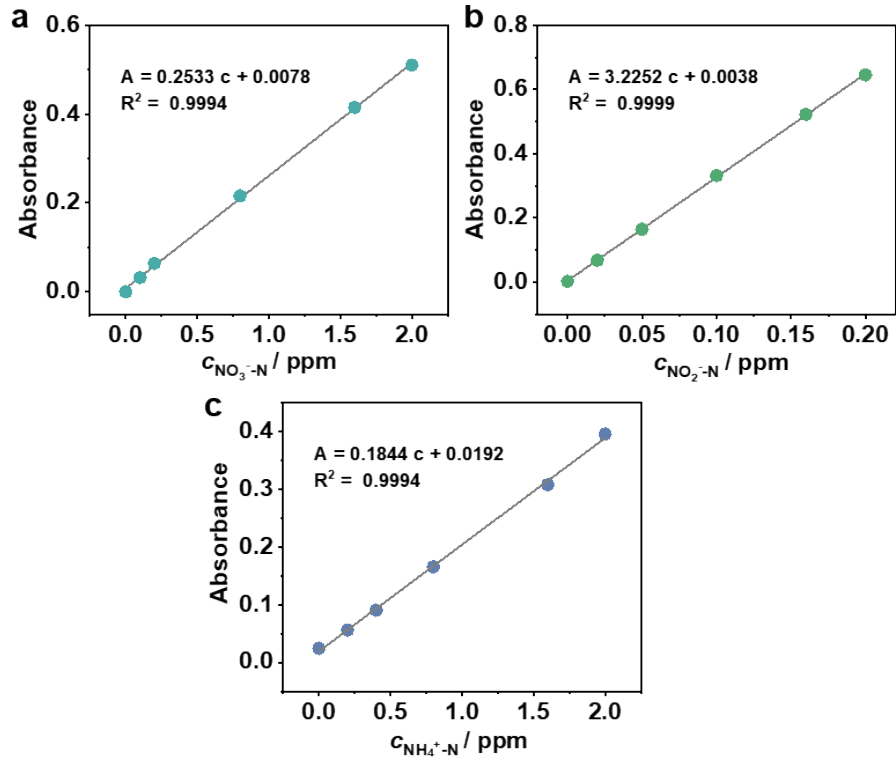
Fig. S11. The concentration-absorbance calibration curves of (a) nitrate-N, (b) nitrite-N and (c) ammonia-N.

The calibration curves all show good linearity.
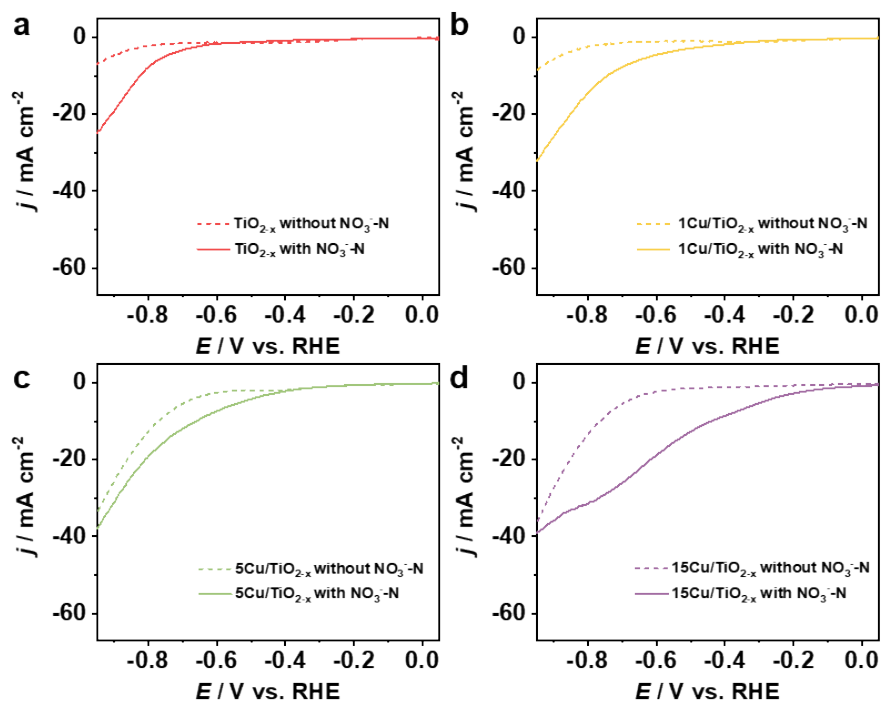
Fig. S12. LSV curves of (a) TiO$_{2-x}$, (b) 1Cu/TiO$_{2-x}$, (c) 5Cu/TiO$_{2-x}$, and (d) 15Cu/TiO$_{2-x}$ in 0.5 M Na$_2$SO$_4$ electrolyte with and without 200 ppm NO$_3^-$-N.

The LSV curves of Cu/TiO$_{2-x}$ samples with different Cu loading amounts all show the enhanced current density in the presence of nitrate, which indicates their ability to reduce nitrate. And among them, 10Cu/TiO$_{2-x}$ exhibits the largest current density in the presence of 200 ppm NO$_3^-$-N.
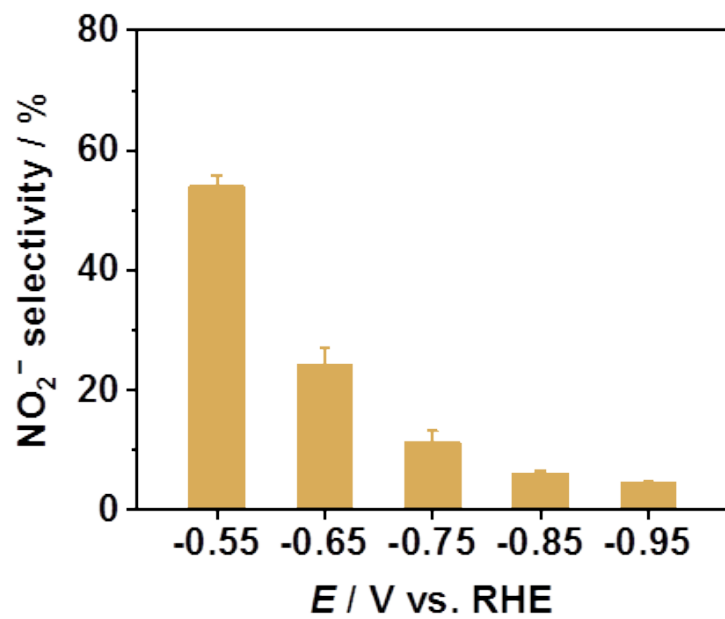
Fig. S13. The selectivity of NO_2^- on 10Cu/TiO_{2-x} at given potentials.

The selectivity to NO_2^- gradually decreased as the potentials become more negative.
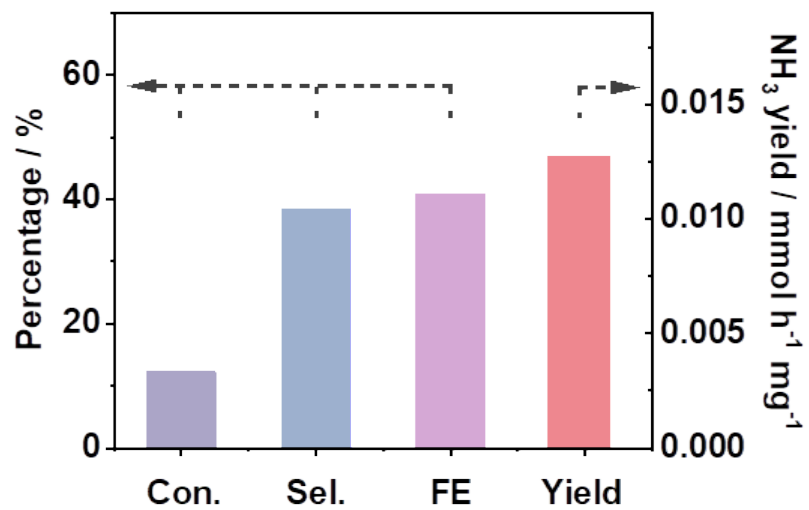
Fig. S14. The electrochemical performance of TiO_2 for nitrate reduction.

Pure TiO_2 shows poor electrochemical performance for NO_3RR with NO_3^- conversion rate of 12.14%, NH_3 selectivity of 38.25%, FE of 40.69%, yield rate of 0.0127 mmol h^{-1} mg^{-1}.
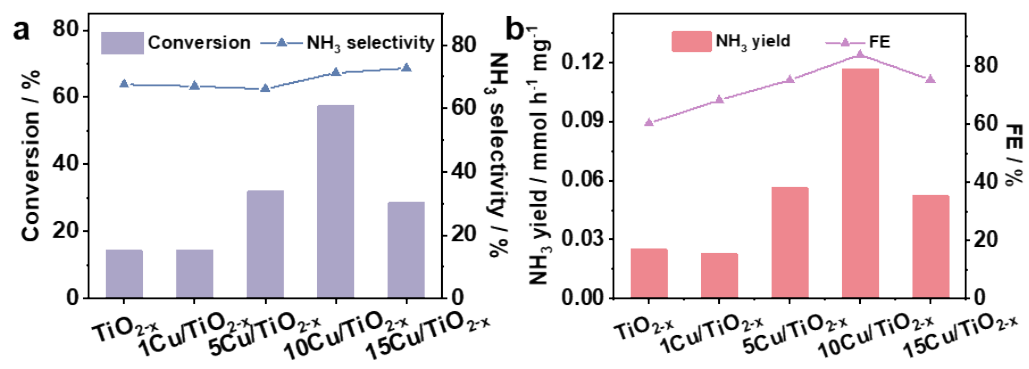
Fig. S15. (a) Conversion rate of nitrate and selectivity to ammonia, (b) yield rate and FE of ammonia on different samples at -0.75 V.
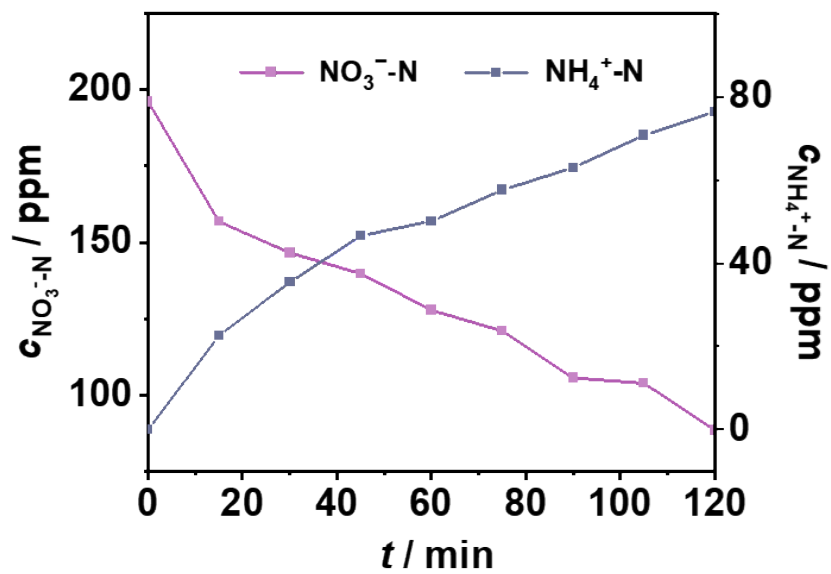
Fig. S16. Time-dependent concentration of nitrate and ammonia on 10Cu/TiO$_{2-x}$ at -0.75 V.
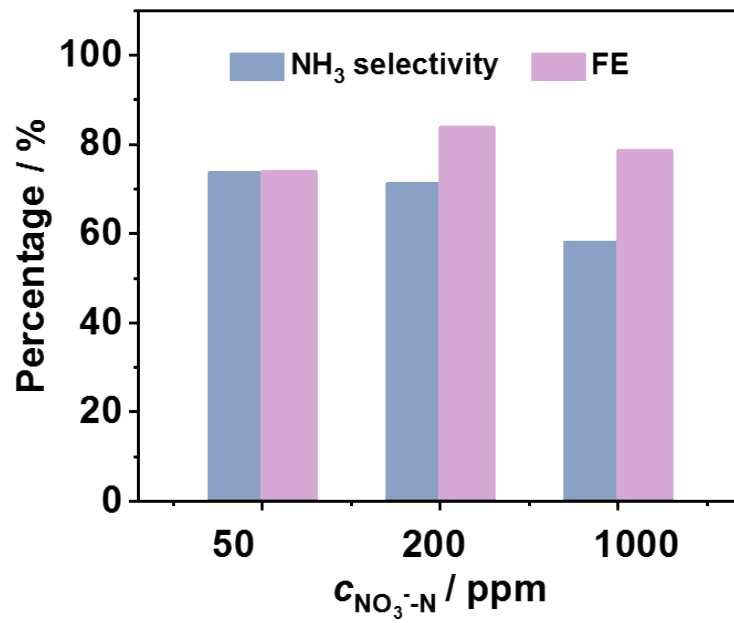
Fig. S17. Selectivity and FE of ammonia for nitrate electroreduction with different nitrate-N concentration on $10Cu/TiO_{2-x}$.
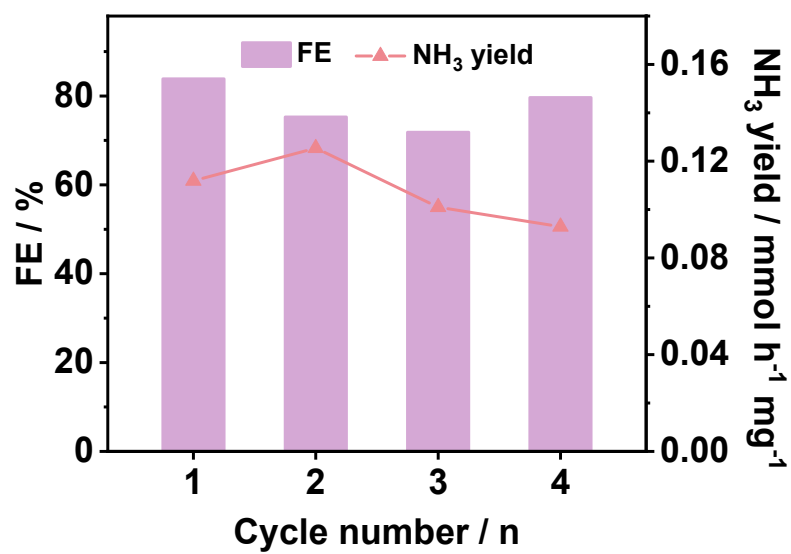
Fig. S18. Long-term durability test at -0.75 V on 10Cu/TiO$_{2-x}$.

During the successive cycling tests, the FE is almost unchanged and yield rate of NH$_3$ shows a slight decay at -0.75 V.
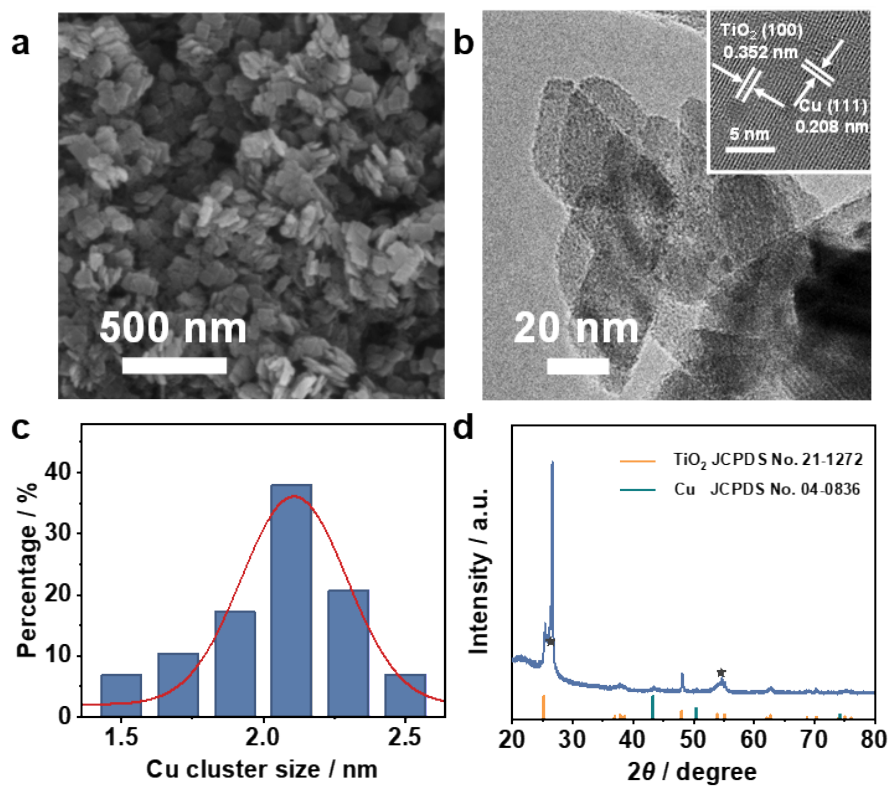
Fig. S19. (a) SEM image, (b) TEM image (inset shows the HRTEM of post-test $10Cu/TiO_{2-x}$, (c) The distribution of the Cu clusters, (d) XRD pattern of post-test $10Cu/TiO_{2-x}$.

The morphology and composition of post-test $10Cu/TiO_{2-x}$ maintain unchanged after the durability test. And the average size of Cu clusters is about 2.14 nm, which is almost unchanged after the electrochemical reaction.
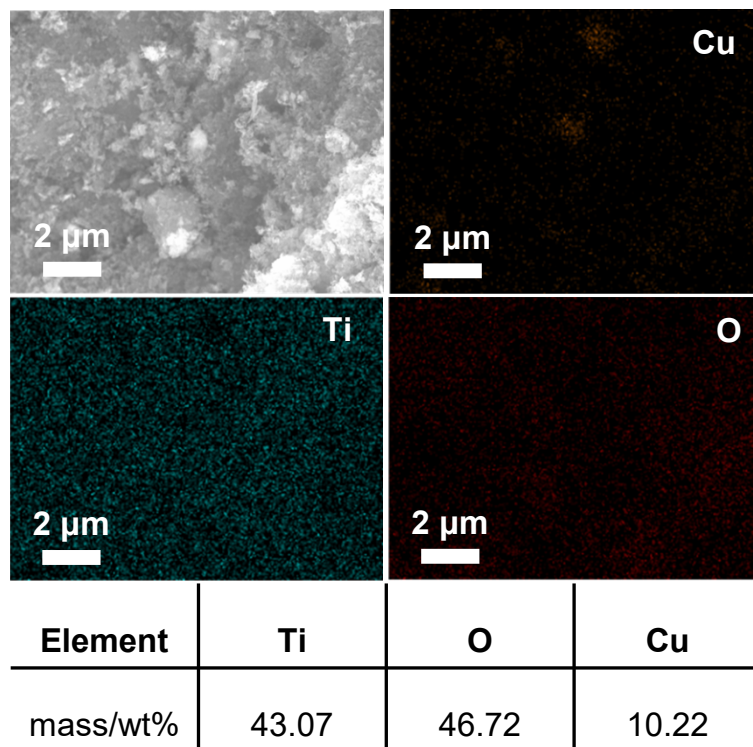
Fig. S20. SEM-EDX mapping image and element content of $10Cu/TiO_{2-x}$ after the durability test.

Element	Ti	O	Cu
mass/wt%	43.07	46.72	10.22

The EDX data suggested the Cu content in $10Cu/TiO_{2-x}$ was about 10.22wt%, implying the stable metal content after the electrochemical NO_3RR.
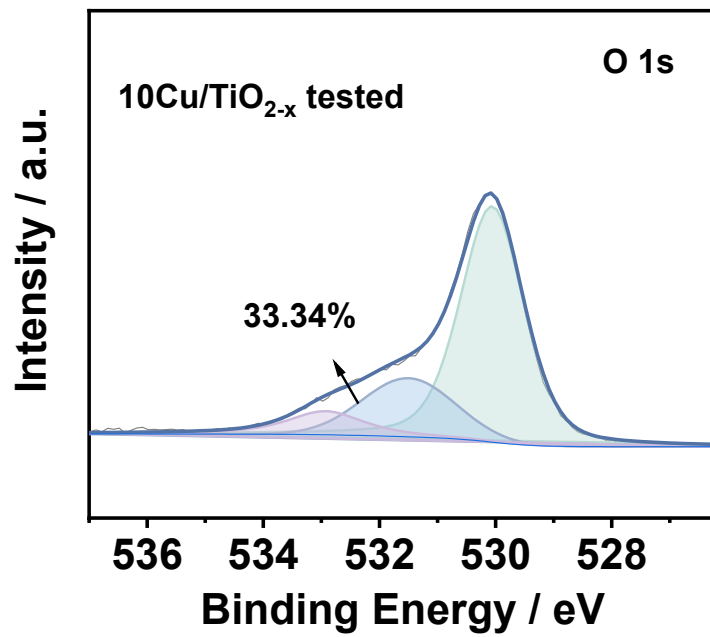
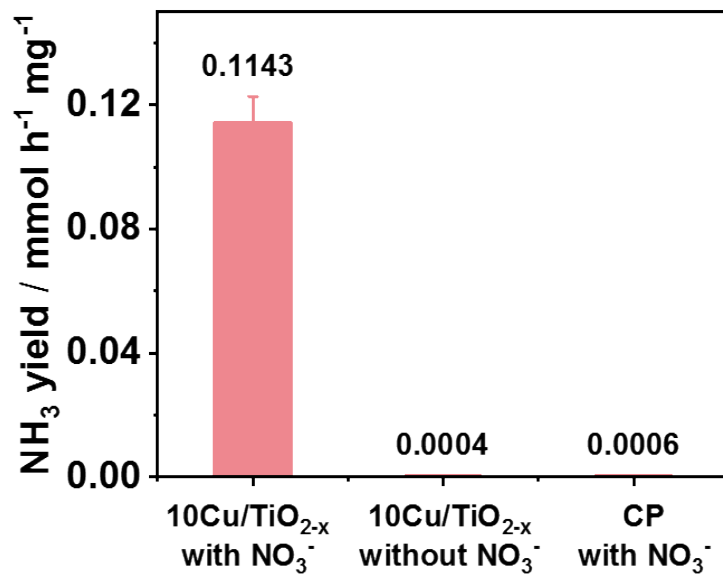**Fig. S21.** O 1s XPS spectrum of post-test 10Cu/TiO$_{2-x}$.

Fig. S22. Ammonia yield rate on 10Cu/TiO$_{2-x}$ in electrolyte with and without nitrate, and on carbon paper in electrolyte with nitrate.

Ignorable ammonia is generated in the comparison tests, which excludes any possible interference from catalyst itself or external environment.
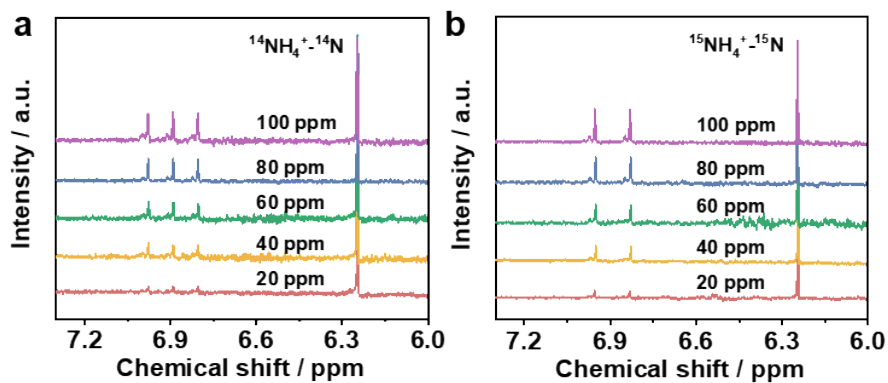
Fig. S23. ^{1}H NMR spectra (600 MHz) of (a) $^{14}NH_4^+$-^{14}N and (b) $^{15}NH_4^+$-^{15}N with different concentrations.

Considering that the peak area of NMR is directly related to ammonia content, the concentration of NH_4^+-N can be quantified by ^{1}H NMR with internal standards (maleic acid). The proton signal of maleic acid appears at $\delta = 6.25$ ppm. The ^{1}H NMR spectra of $^{14}NH_4^+$ show triple peaks at $\delta = 6.98, 6.89, 6.80$ ppm, while that of $^{15}NH_4^+$ show double peaks at $\delta = 6.95, 6.83$ ppm.

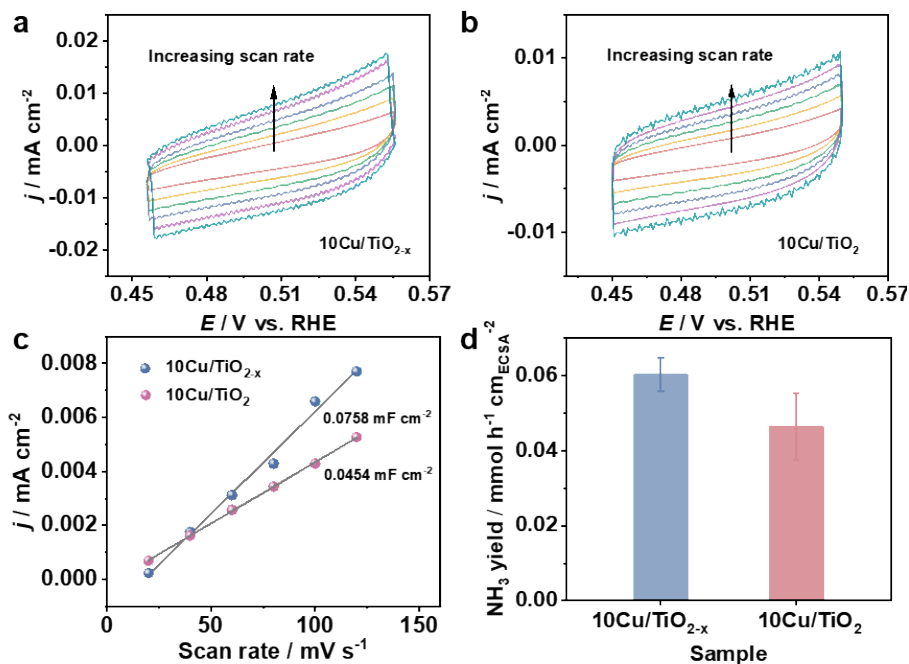**Fig. S24.** Cyclic voltammogram curves of (a) 10Cu/TiO$_{2-x}$ and (b) 10Cu/TiO$_2$ with various scan rates of 20, 40, 60, 80, 100 and 120 mV s^{-1}. (c) Plots of the current density versus the scan rate for 10Cu/TiO$_{2-x}$ and 10Cu/TiO$_2$. (d) The ammonia yield rate normalized to ECSAs for 10Cu/TiO$_{2-x}$ and 10Cu/TiO$_2$.

A linear fit determined the specific capacitance to be 0.0758 mF cm^{-2} for 10Cu/TiO$_{2-x}$ and 0.0454 mF cm^{-2} for 10Cu/TiO$_2$. 40 μF cm^{-2} is assumed as the specific capacitance in the following calculations of electrochemical active surface area (ECSA). The ECSAs is then calculated by the following formula:

$$A_{ECSA}^{10Cu/TiO_2 - x} = \frac{0.0758 \text{ mFcm}^{-2}}{40 \text{ μF cm}^{-2} \text{per cm}_{ECSA}^2} = 1.895 \text{ cm}_{ECSA}^2$$

$$A_{ECSA}^{10Cu/TiO_2} = \frac{0.0454 \text{ mFcm}^{-2}}{40 \text{ μF cm}^{-2} \text{per cm}_{ECSA}^2} = 1.135 \text{ cm}_{ECSA}^2$$

The ammonia yield rate normalized to ECSAs is 0.0603, and 0.0464 mmol h^{-1} cm$_{ECSA}^{-2}$ for 10Cu/TiO$_{2-x}$ and 10Cu/TiO$_2$ samples, respectively. These experimental results confirmed that the enhanced performance of 10Cu/TiO$_{2-x}$ catalyst originates from its higher intrinsic properties than 10Cu/TiO$_2$.
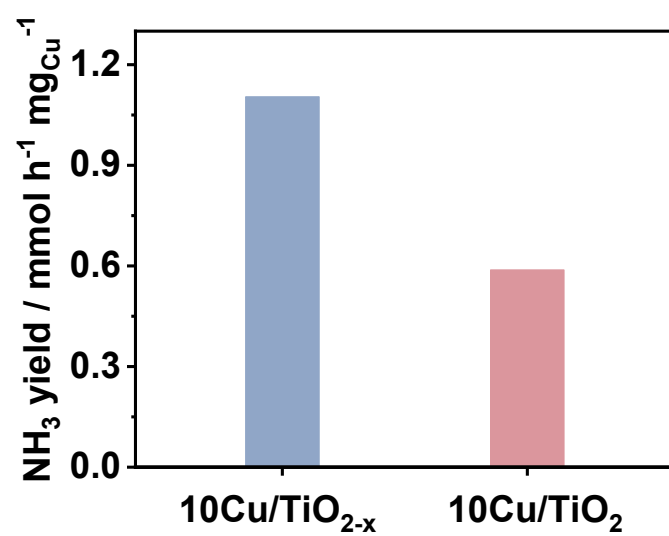
Fig. S25. Yield rate of ammonia normalized to loading amount of Cu for $10Cu/TiO_2$ and $10Cu/TiO_{2-x}$.
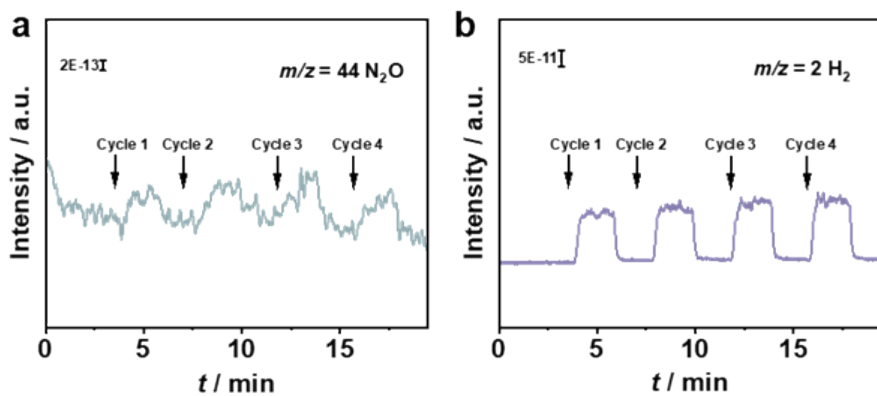
Fig. S26. DEMS measurements of nitrate electroreduction on $10Cu/TiO_{2-x}$.

The by-product of N_2O was also detected during NO_3RR. And the competitive hydrogen evolution reaction also occurs.
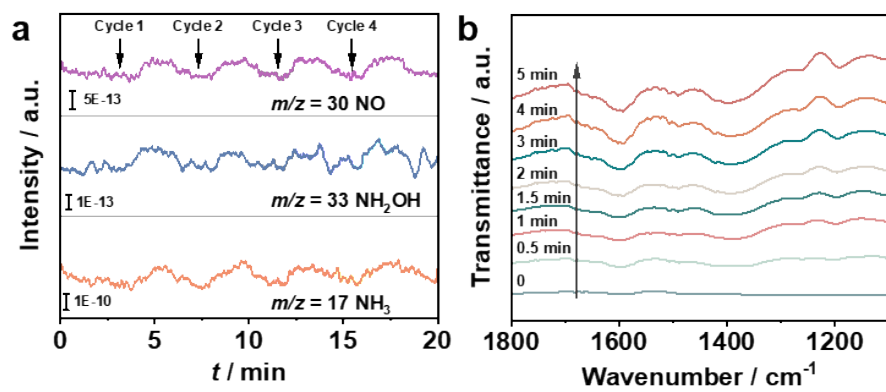
Fig. S27. (a) DEMS measurements of nitrate electroreduction on 10Cu/TiO$_2$. (b) *In situ* FTIR spectra of nitrate electroreduction on 10Cu/TiO$_2$.
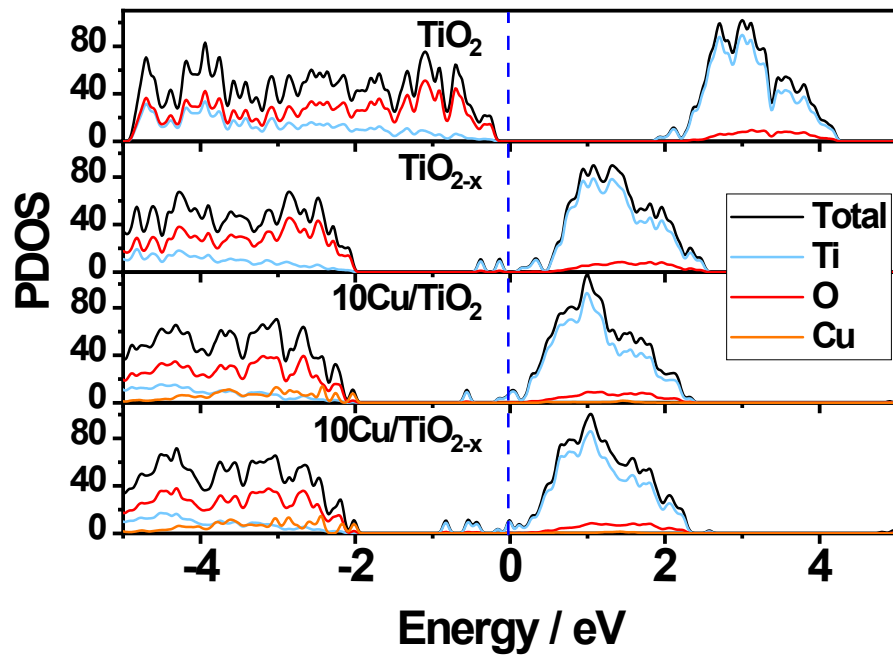
Fig. S28. PDOS of TiO_2, TiO_{2-x}, $Cu-TiO_2$ and $Cu-TiO_{2-x}$.
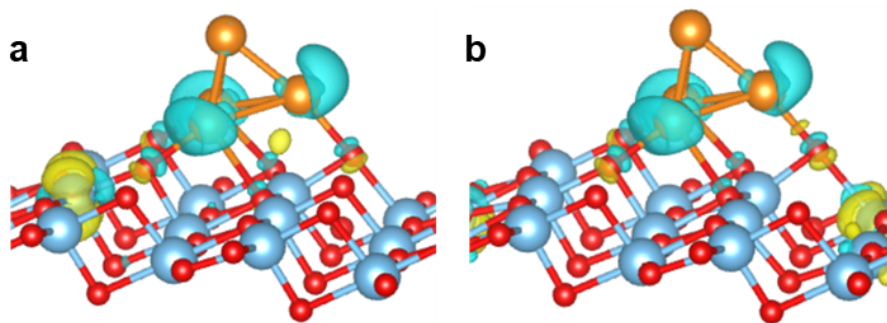
Fig. S29. Isosurfaces of differential charge density of Cu cluster on (a) TiO_2 and (b) TiO_{2-x}. (yellow: electron accumulation; blue: electron depletion. isovalue = 0.01 e/bohr^3)

Fig. S30. Reaction free energy diagram of HER.

Table S1 The actual copper content of different catalysts measured by ICP-OES.

Catalysts	Cu content / wt%
$1Cu/TiO_{2-x}$	0.74
$5Cu/TiO_{2-x}$	4.25
$10Cu/TiO_{2-x}$	10.35
$15Cu/TiO_{2-x}$	15.41
$10Cu/TiO_2$	8.96

Table S2 Comparison of ammonia synthesis from NO_3RR over $10Cu/TiO_{2-x}$ with other reported catalysts.

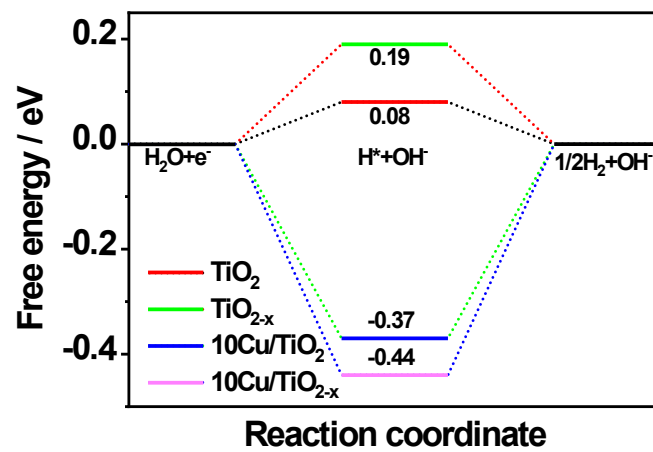| Electrocatalyst	Electrolyte	Performance	Ref.
$10Cu/TiO_{2-x}$	200 ppm NO_3^--N, 0.5 M Na_2SO_4	S_{NH_3}: 73.56% FE_{NH_3}: 81.34% Y_{NH_3}: 0.1143 mmol h^{-1} mg^{-1}	This work
Fe/Cu Composite	100 ppm NO_3^--N, 0.05 M Na_2SO_4	S_{NH_3}: ~70%	[12]
Co_3O_4/Ti	100 ppm NO_3^--N, 0.05 M Na_2SO_4	S_{NH_3}: 32.0%	[13]
Fe_2O_3/Ti	100 ppm NO_3^--N, 0.05 M Na_2SO_4	S_{NH_3}: 50.0%	[13]
TiO_{2-x}	50 ppm NO_3^--N, 0.1 M Na_2SO_4	Y_{NH_3}: 0.045 mmol h^{-1} mg^{-1}	[14]
Ni_2P/NF	80 ppm NO_3^--N, 0.5 M Na_2SO_4	Y_{NH_3}: 0.056 mmol h^{-1} mg^{-1}	[15]
$Co_3O_4@NiO$	200 ppm NO_3^--N, 0.5 M Na_2SO_4	S_{NH_3}: 62.29% FE_{NH_3}: 54.97% Y_{NH_3}: 0.00693 mmol h^{-1} mg^{-1}	[16]
$Co_3O_4-TiO_2$	50 ppm NO_3^--N, 0.1 M Na_2SO_4,	S_{NH_3}: 24%	[17]
$Ni/Fe^0@Fe_3O_4$	50 ppm NO_3^--N, 10 mM NaCl	S_{NH_3}:10.44%	[18]
Cu/rGO/GP	280 ppm NO_3^--N, 0.02 M NaCl	S_{NH_3}: 29.93%	[19]
nZVI@OMC	50 ppm NO_3^--N, 0.02 M NaCl	S_{NH_3}: ~10%	[20]

Pd-Cu/SS	0.6 mM NaNO$_3$, 0.01 M NaClO$_4$	S$_{NH_3}$: 6%	21
Pd-Cu/γAl$_2$O$_3$	50 ppm NO$_3^-$-N	S$_{NH_3}$: 19.6%	22
Pd@Fe$_3$O$_4$@Al$_2$O$_3$	Nitrate from simulated groundwater	S$_{NH_3}$: <5 %	23
Cu incorporated PTCDA	500 ppm of NO$_3^-$-N, 0.1 mM PBS, pH 7	Y$_{NH_3}$: 0.0256 mmol h^{-1} cm^{-2}	24
Blended Sn$_{0.8}$Pd$_{0.2}$/SS	0.008 M NaNO$_3$, 0.1 M HClO$_4$	S$_{NH_3}$: 14%	25

Note:

S$_{NH_3}$: the selectivity of ammonia

FE$_{NH_3}$: the Faradaic efficiency of ammonia;

Y$_{NH_3}$: the yield of ammonia.

Table S3 Ammonia yield on $10Cu/TiO_{2-x}$ determined by different quantitative methods.

Quantitative method	Nitrogen sources	Detected ion	Concentration (ppm)	Yield rate (mmol h^{-1} mg^{-1})
Colorimetric method	$^{14}NO_3^-$	NH_4^+-N	80.01	0.1143
^{1}H NMR	$^{14}NO_3^-$	$^{14}NH_4^+$-^{14}N	79.35	0.1134
^{1}H NMR	$^{15}NO_3^-$	$^{15}NH_4^+$-^{15}N	77.95	0.1114

The yields of $^{14}NH_4^+$ and $^{15}NH_4^+$ determined by ^{1}H NMR are very close to the results of colorimetric method.

Reference

1. J. Wan, W. Chen, C. Jia, L. Zheng, J. Dong, X. Zheng, Y. Wang, W. Yan, C. Chen, Q. Peng, D. Wang and Y. Li, *Adv. Mater.*, 2018, **30**, 1705369.

2. C. Chen, X. Zhu, X. Wen, Y. Zhou, L. Zhou, H. Li, L. Tao, Q. Li, S. Du, T. Liu, D. Yan, C. Xie, Y. Zou, Y. Wang, R. Chen, J. Huo, Y. Li, J. Cheng, H. Su, X. Zhao, W. Cheng, Q. Liu, H. Lin, J. Luo, J. Chen, M. Dong, K. Cheng, C. Li and S. Wang, *Nat. Chem*, 2020, **12**, 717-724.

3. G. Kresse and J. Furthmüller, *Comput. Mater. Sci.*, 1996, **6**, 15-50.

4. G. Kresse and J. Furthmüller, *Phys Rev B Condens Matter*, 1996, **54**, 11169-11186.

5. K. Glantschnig and C. Ambrosch-Draxl, *New J. Phys.*, 2010, **12**, 103048.

6. S. L. Dudarev, G. A. Botton, S. Y. Savrasov, C. J. Humphreys and A. P. Sutton, *Phys. Rev. B*, 1998, **57**, 1505-1509.

7. H. Xu, D. Cheng, D. Cao and X. C. Zeng, *Nat. Catal.*, 2018, **1**, 339-348.

8. K. Mathew, R. Sundararaman, K. Letchworth-Weaver, T. A. Arias and R. G. Hennig, *J Chem. Phys.*, 2014, **140**, 084106.

9. J. K. Nørskov, J. Rossmeisl, A. Logadottir, L. Lindqvist, J. R. Kitchin, T. Bligaard and H. Jónsson, *The Journal of Physical Chemistry B*, 2004, **108**, 17886-17892.

10. M. Sturzenegger, N. Prokopuk, C. N. Kenyon, W. J. Royea and N. S. Lewis, *J Phys. Chem. B*, 1999, **103**, 10838-10849.

11. W. A. Chupka, J. Berkowitz and D. Gutman, *J Chem. Phys.*, 1971, **55**, 2724-2733.

12. Y. Zhang, Y. Zhao, Z. Chen, L. Wang, L. Zhou, P. Wu, F. Wang and P. Ou, *J. Electrochem. Soc.*, 2018, **165**, E420-E428.

13. L. Su, K. Li, H. Zhang, M. Fan, D. Ying, T. Sun, Y. Wang and J. Jia, *Water Res.*, 2017, **120**, 1-11.

14. R. Jia, Y. Wang, C. Wang, Y. Ling, Y. Yu and B. Zhang, *ACS Catal.*, 2020, **10**, 3533-3540.

15. Q. Yao, J. Chen, S. Xiao, Y. Zhang and X. Zhou, *ACS Appl. Mater. Interfaces*, 2021, **13**, 30458-30467.

16. Y. Wang, C. Liu, B. Zhang and Y. Yu, *Sci. China Mater.*, 2020, **63** 2530-2538.

17. J. Gao, B. Jiang, C. Ni, Y. Qi, Y. Zhang, N. Oturan and M. A. Oturan, *Appl. Catal., B*, 2019, **254**, 391-402.

18. Z. A. Jonoush, A. Rezaee and A. Ghaffarinejad, *J Cleaner Prod.* 2020, **242**, 118569.

19. D. Yin, Y. Liu, P. Song, P. Chen, X. Liu, L. Cai and L. Zhang, *Electrochim. Acta*, 2019, **324**, 134846.

20. W. Teng, N. Bai, Y. Liu, Y. Liu, J. Fan and W. X. Zhang, *Environ. Sci. Technol.*, 2018, **52**, 230-236.

21. J. F. Su, I. Ruzybayev, I. Shah and C. P. Huang, *Appl. Catal., B*, 2016, **180**, 199-209.

22. Z. Zhang, Y. Xu, W. Shi, W. Wang, R. Zhang, X. Bao, B. Zhang, L. Li and F. Cui, *Chem. Eng. J.*, 2016, **290**, 201-208.

23. E. Rahimi, G. Sajednia, M. Baghdadi and A. Karbassi, *J. Environ. Chem. Eng.,* 2018, **6**, 5249-5258.

24. G.-F. Chen, Y. Yuan, H. Jiang, S.-Y. Ren, L.-X. Ding, L. Ma, T. Wu, J. Lu and H. Wang, *Nat. Energy*, 2020, **5**, 605-613.

25. J. F. Su, W.-F. Kuan, H. Liu and C. P. Huang, *Appl. Catal., B*, 2019, **257**, 117909.